Additive Manufacturing 46 (2021) 102078

Contents lists available at ScienceDirect

Additive Manufacturing

journal homepage: www.elsevier.com/locate/addma

Research Paper

# Iterative simulation-based techniques for control of laser powder bed fusion additive manufacturing

Jeff E. Irwin [a,b,*], Qian Wang [a], Panagiotis (Pan) Michaleris [d], Abdalla R. Nassar [c], Yong Ren [a], Christopher B. Stutzman [c]

[a] Department of Mechanical Engineering, The Pennsylvania State University, University Park, PA 16802, USA
[b] Autodesk Inc., 200 Innovation Park, State College, PA 16803, USA
[c] Applied Research Laboratory, The Pennsylvania State University, University Park, PA 16802, USA
[d] Independent researcher

ARTICLE INFO

*Keywords:*
Laser powder bed fusion
Finite element analysis
Numerical methods
Process control

ABSTRACT

One of the challenges for process control of laser powder bed fusion additive manufacturing lies in thermal control. Excessively low laser power may lead to incomplete melting, while too high laser power can lead to keyholing, increasing the porosity of parts. Considering a thermal finite-element model from our prior work, a secant-based iterative method is proposed and implemented in this work to control the simulated laser power to attain a constant melt-pool size. Several experimental samples of Inconel 625 are designed and built with the EOSINT M280 system, and cross-sectioned to evaluate the effectiveness of the iterative simulation-based controller of laser power. Cross-sectional area statistics are collected near laser turnarounds, where the melt pool is most dynamic. The iterative simulation-based controller reduces the variation of melt pool size by between 13.4% and 48.8% compared to applying constant laser power for all configurations. With the extra iterations from the secant method, the controlled simulations take roughly 2.3 times longer than the simulations under constant laser power.

## 1. Introduction

Laser powder-bed fusion (LPBF) is a manufacturing process which builds up a part layer by layer. Layers are thin, usually less than 100 $\mu$m, allowing parts of high geometric complexity to be created [1]. The process is innovative as many LPBF parts cannot be built with traditional manufacturing methods [2]. However, several failure modes can occur during the LPBF process [3], including high residual stress and distortion [4]. Another challenge of LPBF lies in thermal control, which can result in porosity or lack-of-fusion defects in the final part [5].

Lack of fusion [6], also known as incomplete melting [7], occurs at too-low energy densities. Overheating [8], on the other hand, occurs at too-high energy densities and may cause keyholing. Over melting is a similar but less extreme defect, classified differently from overheating by reference [7]. Both of these defects result in porosity. The optimal energy density that minimizes porosity is somewhere in the middle between the two defect regimes [6,7]. Other defects such as an undesirable microstructure can weaken mechanical properties [9]. This work focuses on defects related to temperature itself, not microstructure, which is also driven by rate of cooling [10].

Process maps have been used to optimize manufacturing processes [11], where suitable process parameters such as powers and scan speeds are searched by experimental trial and error [12,13,4]. Beuth et al. have also used simulations to construct process maps [14]. Note that builds may be divided into several regions, such as upskin, downskin, contour, and infill, each with their own process parameters [15,16]. Processing parameters that work well for one region may not work as well for other regions. Further, the optimal processing parameters may change during the build process. For example, if one layer becomes too hot, the next layer may need to be deposited at a lower energy density. For a finer-scale (than bulk) process map, some researchers monitor the melt pool in real-time to control the laser power [17]. However, such in-situ monitoring requires special instrumentation and extensive modification to the LPBF system. Another method for mitigating thermal-related defects is the use of support structures. Besides their mechanical application for holding a part in place, support structures can be added as a path for heat conduction to alleviate hot spots. However, the design of support structures creates additional challenges. For example, although

* Corresponding author at: Department of Mechanical Engineering, The Pennsylvania State University, University Park, PA 16802, USA.
*E-mail address:* jei5028@psu.edu (J.E. Irwin).

https://doi.org/10.1016/j.addma.2021.102078
Received 23 January 2021; Received in revised form 30 April 2021; Accepted 26 May 2021
Available online 9 June 2021

supports can be added automatically by a metric based on the overhang angle, they often need to be modified through trial and error. One limitation of all thermal control methods is that defects are not only related to the printing parameters and melt pool characteristics. For example, spatter from a previous weld can cause porosity on a subsequent track. Even when operating in ideal conditions within the process window it is possible to obtain defects.

Several researchers have conducted process control for directed energy deposition (DED) processes. Toyserkani and Khajepour used a camera to monitor and control build height and showed improved geometric characteristics in a thin wall built by a laser powder deposition process [18]. Song et al. used cameras and pyrometers to monitor a direct metal deposition process to control build height and melt pool temperature [19]. Tang and Landers controlled melt pool temperature, but they found that it did not necessarily improve deposition quality for the laser metal deposition process [20]. Similar to this work, several other researchers have implemented feed-forward controllers [21–23]. Cao and Ayalew implemented a controller for layer height and melt pool temperature in COMSOL, but they did not experimentally validate their model [24,25]. Wang et al. implemented a controller for melt pool height and temperature [26] and later validated the controller experimentally, demonstrating improved accuracy in build height [27]. DED processes have different process control inputs from LPBF processes, e.g. powder flow rate is unique in DED; and in addition, models and boundary conditions are different for these two types of AM processes. Hence, the process control for DED cannot be directly transferred to LPBF processes.

For process control of LPBF, one notable work was conducted by Druzgalski et al., where a feature-based controller was implemented to reduce power in abrupt step changes based on criteria of how close a scan is to an overhang or a turnaround [22]. They noted that overhangs had a better surface finish with less debris after applying their controller. However, the validation is qualitative and based on global properties such as porosity and dross formation, rather than on localized defects at individual turnarounds. Yeung et al. proposed a geometric conductance factor (GCF) controller for reducing laser power in the vicinity of less-conductive powder, both at edges within a layer and above overhangs in lower layers [23]. Like Druzgalski's controller, the GCF controller is based on a geometric heuristic and is not directly tied to a thermal model of the process.

Papacharalampopoulos et al. performed multi-criteria optimization to regulate melt pool depth as well as keep the maximum temperature below boiling and keep the cooling rate within prescribed limits during several phases of the laser AM process [28]. However, they did not show their results with multiple tracks or validate against experimental measurements. Khairallah et al. implemented a PID controller in a high-fidelity multi-physics model of the LPBF process [29]. Although the multi-physics model can capture a high level of detail of the process, it is not as fast as a solid-phase thermal FEA model and thus not as practical for larger toolpaths in real parts.

Analytic models based on Rosenthal's work [30] have been used for process control of LPBF [31]. Numeric solutions from finite element analysis (FEA) have many advantages over the analytic Rosenthal solution. For example, FEA can model various kinds of non-linearities, such as temperature-dependent material properties, loose powder, as well as complex laser paths, to name a few. For certain types of laser paths, the Rosenthal solution can use "imaginary" [32] or "virtual" [33] heat sources, but it does not scale. The Rosenthal solution can use symmetry for an insulated boundary condition (BC) on a plane [34,35], but it cannot model more complex BCs. Finally, the Rosenthal solution is a steady-state solution. Even with a transient modification [35] it cannot model the increase in melt volume at the beginning of a track.

This work focuses on using FEA-based simulation method to control processing parameters in order to attain thermal objectives, where the regulation of melt-pool volume (or cross-sectional area) is used as a heuristic for avoiding porosity and lack of fusion. If an FEA model only accounts for heat conduction in a solid, but not fluid mechanics or vaporization, then it will not be able to directly predict keyholing. However, it is possible to control the process parameters to maintain the melt pool in the regime where the assumption of heat conduction holds and no keyholing will appear.

In this work, the thermal finite-element model from reference [36] is applied to the LPBF process. Then the secant method is used to iteratively control the simulated laser power in the FEA to attain a constant melt pool volume. Sensitivity study of the FEA model with respect to multiple simulation parameters are conducted. The accuracy of the FEA melt-pool prediction is validated with single beads scanned with constant laser power. For experimental evaluation, the laser-power trajectory from the FEA controller is implemented on an EOSINT M280 LPBF system for the fabrication of multi-hatch parts of Inconel 625. The effectiveness of the controller is evaluated by measuring variations in cross-sections.

## 2. Finite element formulation and secant-based iterative control of laser power

### 2.1. Transient thermal analysis

For transient heat conduction analysis in a volume $V$ with boundary $S$, the governing energy balance equation at all points in $V$ is:

$$\rho C_p \frac{\partial T}{\partial t} = \nabla\cdot(k\nabla T) + Q \tag{1}$$

where $\rho$ is the mass density, $C_p$ is the constant-pressure specific heat, $T$ is the temperature field, $t$ is time, $k$ is the temperature-dependent thermal conductivity matrix, $Q$ is the volumetric internal heat generation rate. The operator $\nabla$ [1/mm] is given by:

$$\nabla = \left[\frac{\partial}{\partial x} \quad \frac{\partial}{\partial y} \quad \frac{\partial}{\partial z}\right]^{\mathrm{T}} \tag{2}$$

where $x$, $y$, and $z$ are Cartesian spatial coordinates and $(\cdot)^{\mathrm{T}}$ represents the matrix transpose operation.

For the initial condition of the heat transfer problem, consider an initial temperature field $T = T_0$ at an initial time $t = t_0$ throughout the volume $V$ of the part. The boundary conditions consist of prescribed temperatures $T_{\mathrm{p}}$ and prescribed heat fluxes $q_{\mathrm{p}}$, on two disjoint surfaces:

$$T = T_{\mathrm{p}} \quad \text{on surface } S_T \text{ for all } t \tag{3}$$

$$-k\nabla T\cdot\mathbf{n} = q_{\mathrm{p}} \quad \text{on surface } S_q \text{ for all } t \tag{4}$$

where the two surfaces $S_T$ and $S_q$ satisfy the relations $S_T \bigcup S_q = S$ and $S_T \bigcap S_q = \varnothing$; $\mathbf{n}$ denotes the unit normal vector pointing outward to the surface.

Using the Galerkin approach, the energy balance in Eq. (1) can be converted to a weak formulation. In conjunction with an appropriate finite element discretization, this formulation results in a nodal temperature vector $\mathbf{T}$, a residual vector $\mathbf{R}$, and a stiffness matrix $\mathrm{d}\mathbf{R}/\mathrm{d}\mathbf{T}$. From an initial estimate of temperatures $\mathbf{T}^0$, the Newton-Raphson method can be iteratively applied:

$$\mathbf{T}^{i+1} = \mathbf{T}^i - \left[\frac{\mathrm{d}\mathbf{R}^i}{\mathrm{d}\mathbf{T}}\right]^{-1}\mathbf{R}^i \tag{5}$$

where the superscripts $i$ and $i+1$ refer to the previous and current iterations. Eq. (5) is applied until an appropriate norm of the residual $\mathbf{R}$ is less than some specified tolerance. The thermal analysis is performed in the finite element software, Autodesk's Netfabb Local Simulation. Further details of the finite element formulation can be found in references [36,37].

### 2.2. Secant-based iterative control of laser power in FEA

This work proposes a secant-based method to compute the simulated laser power in FEA and iteratively repeats each time increment until the target melt-pool volume is attained. At each iteration $i$, the secant method is used with the powers $P$ and melt volumes $V$ from the two previous iterations at $i-1$ and $i-2$ to converge towards the optimal power:

$$P_i = P_{i-1} - \frac{(P_{i-2} - P_{i-1})(V_{i-1} - V_{\text{target}})}{V_{i-2} - V_{i-1}} \tag{6}$$

where the melt volumes $V$ under the laser powers $P$ are computed by the finite-element solver.

A schematic of the secant method iteration is shown in Fig. 1 along with a hypothetical underlying $V$ vs $P$ function. Due to the discrete nature of the melt pool volume quadrature, a derivative-based root finding method may be ill-conditioned on this underlying function. The secant method is well suited for this function and it is simple to implement. This controller results in smooth changes in power that rise gradually coming out of each turnaround.

The secant iterations of Eq. (1) are performed outside of the Newton-Raphson iterations of Eq. (5), but inside of each time increment. The simulation does not proceed to the next time increment until after the secant method converges.

## 3. Experimental methods

In order to evaluate the effectiveness of the FEA controller of laser power derived in Sec. 2.2, a set of bead-on-plate experimental samples of Inconel 625 was designed, built and cross-sectioned. The samples are built using an EOSINT M280 laser powder bed system. For the FEA controller of laser power, the laser-power trajectory output by the FEA simulation with secant-iteration of laser power is implemented as a feed-forward control to vary laser power in the AM system. The performance of the FEA control of laser power is then compared to the analytic controller from reference [31], and both are benchmarked against applying a constant laser power of 250 W in scanning the parts.

For the constant-power strategy, samples of 1-bead, 2-bead, and 5-bead are built. For the FEA and analytic laser-power strategy, only samples of 2-bead and 5-bead are built, as modulating of laser-power is needed only during the second track and the subsequent tracks to compensate for thermal accumulation from past tracks. An alternating back-and-forth scan pattern is used for multi-bead samples, as illustrated in Fig. 2 for the 5-bead samples. The laser beam radius is $r = 0.075$ mm,

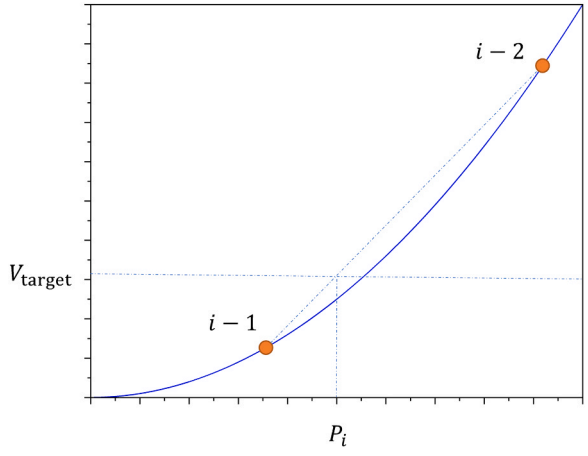


**Fig. 1.** A single iteration of the secant method, finding a new power $P_i$ from the previous two powers and volumes at iterations $i-2$ and $i-1$. The solid curve represents the hypothetical function of volume with respect to power.

and the hatch spacing $\Delta y = 0.1$ mm. Two laser scan speeds, $v = 800$ mm/s and $v = 600$ mm/s, as well as three different track lengths of 5 mm, 10 mm, and 20 mm, are investigated. In between beads, the laser is turned off for a duration equal to $\Delta y/v$ while it repositions. To assess the repeatability and statistical variation due to stochastic factors, each group, corresponding to each combination of process parameters and build configuration (track length and number of tracks), is repeated identically 4 times. The build layout for all the scans is shown in Fig. 3(a) and 3(b). All samples are built on a single Inconel 625 plate with a dimension of 250 mm × 250 mm × 6.35 mm. Each experiment (under one set of process parameters) is spaced 5 mm from the next to minimize heat conduction between groups of beads.

Constant laser-power cases are built with the default EOSINT AM system software. For the controlled laser-power cases, a man-in-the-middle strategy is used, where the commanded nominal laser power is intercepted by the ARL DAQ-SC system (developed at the Penn State Applied Research Lab) and replaced with the controlled laser power, similar to that described in [16,31]. Typical rise times for the utilized laser system (IPG YLR Fiber laser) are on the order of 10 $\mu$s. Modulation of laser power/trigger at 50 kHz (20 $\mu$s) is standard. The smallest FEA time increment is $\Delta t = 46.9\mu$s, hence the laser hardware is capable of performing at the speed required by the FEA controller.

All experimental cases are described in Tables 1, 2, and 3 respectively for constant power, FEA control, and analytic control. The first part of the case ID, either an uppercase letter or number, uniquely identifies the experimental build parameters listed in Tables 1–3. For example, case B uses constant laser power and a scan speed of 800 mm/s, with 2 tracks, each 20 mm long. The second part of the case ID, after a hyphen (-), is a number for experimental repetitions. As an example, B-1, B-2, B-3, and B-4 are four identical builds repeated with the same parameters. Any variation in the results of these cases is due to stochastic factors. In addition to stochastic events which are a normal part of the process, sometimes there are obvious errors in the build. For example, with case Q, only Q-2 and Q-4 are valid. An observation of the build data showed that both cases Q-1 and Q-3 scanned two beads in the same direction instead of alternating directions. This was a consequence of the inability to dictate individual bead trajectory within the AM system software. Such samples built with errors are excluded from the results for comparison.

All samples are cross-sectioned at 1 mm from each end of the track. Then the four repeated samples within each group are mounted in a single specimen for polishing and etching with metallographic techniques to obtain images of melt-pool cross-sections. Melt-pool cross-sectional areas, depths, and widths are obtained from imaging processing.

The effectiveness of the three types of laser-power strategies is evaluated by measuring the cross-sectional areas at 1 mm from the beginning and end of each scan. The constant-power cases are expected to have a higher variation in areas, particularly, larger areas just after a turnaround. Unlike the global surface finish validation performed by Druzgalski et al. [22], this cross-section validation is local and thus can evaluate the controller at specific points in space.

## 4. Results and discussion

### 4.1. Sensitivity study

The effectiveness of any model-based controller is dependent on the accuracy of the model. Several simulation parameters of the FEA model are studied and calibrated. These parameters include: .

- The size of the simulation domain extending into the substrate $\Delta x_s$
- The number of fine layers $n$ in the FEA mesh
- Goldak parameters including heat source depth $d$ [38] and heat source absorption efficiency $\eta$

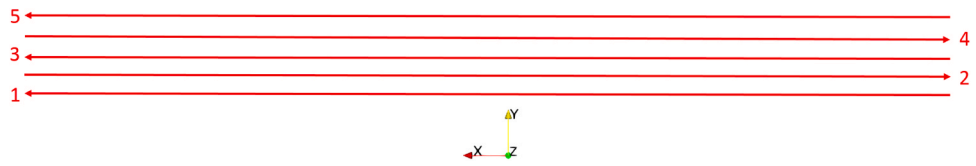


**Fig. 2.** Laser scan pattern for the 5-bead experiment, not to scale, showing the sequence and alternating direction of the beads.

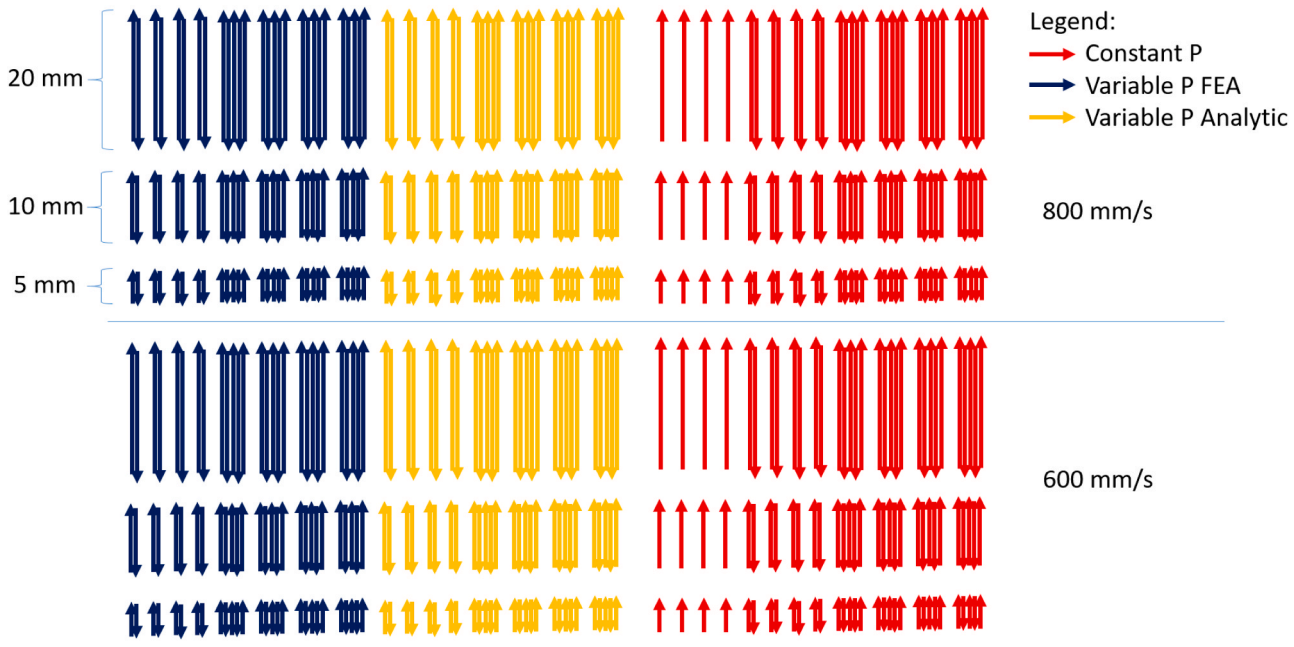


(a)

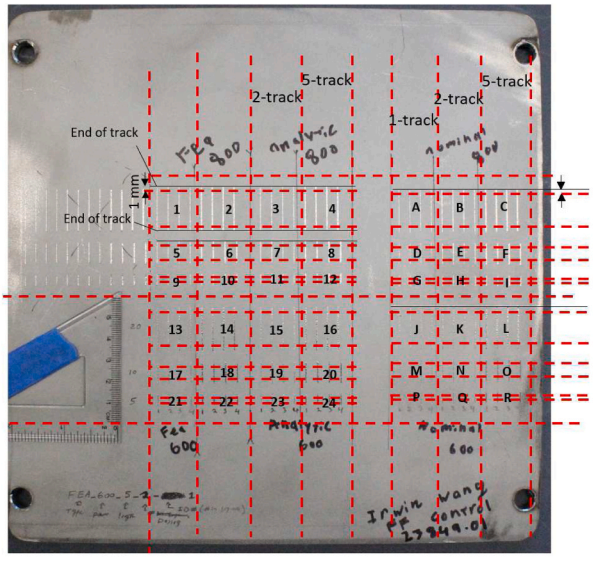


(b)

**Fig. 3.** Build plate schematic (not to scale) 3(a) and actual layout 3(b), including experiments with different power control strategies, bead lengths, scan speeds, and number of beads per group.

- High-temperature conductivity properties approximating Marangoni convection (conductivity multiplication factor)

All of the simulation cases for the sensitivity study and their associated parameters are summarized in Table 4. As before, the first part of the case ID before the hyphen (-) uniquely identifies the experimental build parameters from Tables 1 to 3, including the power profile, laser scan speed, number of tracks, and track length. The second part of the case ID, after a hyphen, is a lowercase letter representing a sensitivity study of multiple simulation parameters for the same experimental case. For example, cases H-a, H-b, and H-c are three different simulation models of experimental case H (constant power of 250 W, 800 mm/s, 2

**Table 1**
Description of the constant power (250 W) experimental cases.

| Case ID | Scan Speed (mm/s) | Number of tracks | Track length (mm) | Valid samples |
|---|---|---|---|---|
| A | 800 | 1 | 20 | – |
| B | 800 | 2 | 20 | B-1, B-2, B-3, B-4 |
| C | 800 | 5 | 20 | – |
| D | 800 | 1 | 10 | D-1, D-2, D-3, D-4 |
| E | 800 | 2 | 10 | E-2, E-4 |
| F | 800 | 5 | 10 | F-1, F-2, F-3, F-4 |
| G | 800 | 1 | 5 | – |
| H | 800 | 2 | 5 | – |
| I | 800 | 5 | 5 | – |
| J | 600 | 1 | 20 | – |
| K | 600 | 2 | 20 | – |
| L | 600 | 5 | 20 | – |
| M | 600 | 1 | 10 | M-1, M-2, M-3, M-4 |
| N | 600 | 2 | 10 | N-1, N-2, N-3, N-4 |
| O | 600 | 5 | 10 | O-1, O-2, O-3, O-4 |
| P | 600 | 1 | 5 | P-1, P-2, P-3, P-4 |
| Q | 600 | 2 | 5 | Q-2, Q-4 |
| R | 600 | 5 | 5 | R-1, R-2, R-3 |

**Table 2**
Description of the FEA controlled experimental cases.

| Case ID | Scan Speed (mm/s) | Number of tracks | Track length (mm) | Valid samples |
|---|---|---|---|---|
| 1 | 800 | 2 | 20 | – |
| 2 | 800 | 5 | 20 | – |
| 5 | 800 | 2 | 10 | 5–1, 5–2, 5–3, 5–4 |
| 6 | 800 | 5 | 10 | 6–1, 6–2, 6–4 |
| 9 | 800 | 2 | 5 | 9–1, 9–2, 9–4 |
| 10 | 800 | 5 | 5 | 10–1, 10–2, 10–3, 10–4 |
| 13 | 600 | 2 | 20 | – |
| 14 | 600 | 5 | 20 | – |
| 17 | 600 | 2 | 10 | 17–1, 17–2, 17–3, 17–4 |
| 18 | 600 | 5 | 10 | 18–1, 18–2, 18–3, 18–4 |
| 21 | 600 | 2 | 5 | 21–1, 21–2, 21–4 |
| 22 | 600 | 5 | 5 | 22–1, 22–2, 22–3, 22–4 |

**Table 3**
Description of the analytic controlled experimental cases.

| Case ID | Scan Speed (mm/s) | Number of tracks | Track length (mm) | Valid samples |
|---|---|---|---|---|
| 3 | 800 | 2 | 20 | – |
| 4 | 800 | 5 | 20 | – |
| 7 | 800 | 2 | 10 | 7–2, 7–4 |
| 8 | 800 | 5 | 10 | 8–1, 8–2, 8–3, 8–4 |
| 11 | 800 | 2 | 5 | – |
| 12 | 800 | 5 | 5 | – |
| 15 | 600 | 2 | 20 | – |
| 16 | 600 | 5 | 20 | – |
| 19 | 600 | 2 | 10 | – |
| 20 | 600 | 5 | 10 | 20–1, 20–2, 20–3, 20–4 |
| 23 | 600 | 2 | 5 | 23–1, 23–2, 23–4 |
| 24 | 600 | 5 | 5 | 24–1, 24–2, 24–3, 24–4 |

tracks, 5 mm), but each model has a different substrate extension length $\Delta x_s$. The sensitivity study is first conducted with respect to the constant power profile of 250 W (Sec. 4.1.2–Sec. 4.1.4), and then conducted with respect to the FEA controlled laser power profile (Sec. 4.1.5).

The conductivity properties used in the FEA are shown in Fig. 4, which are based on references [39,40]. Temperature-dependent specific heat for Inconel®625 is also shown in Fig. 4. The density for Inconel®625 is $\rho = 8.44 \times 10^{-6}$ kg/mm$^3$.

#### 4.1.1. Nominal simulation parameters

The nominal simulation parameters used for the FEA model are defined as follows: substrate extension $\Delta x_s = 0$ mm, number of fine layers $n = 4$, Goldak depth $d = 0.6$ [41], Goldak efficiency $\eta = 0.4$ [42–44], and conductivity multiplication factor 4 for Marangoni modeling. These nominal conditions are referred to "-a" cases in Table 4. In addition, these nominal simulation parameters are used to generate the laser power profiles for experimental validation of the FEA controller.

#### 4.1.2. Mesh sensitivity study

First, the sensitivity of the FEA model prediction with respect to the size of the simulation domain is studied. Case H is chosen as the basis of this study because the shorter 5 mm tracks can be simulated quickly with many subcases. Fig. 5 illustrates the three different cases of the substrate extension being considered, with $\Delta x_s = 0$ mm, 1 mm, and 5 mm, corresponding to case H-a, H-b, and H-c respectively.

Fig. 6 shows the automatically-generated static mesh for case H-a with the number of fine layers $n = 4$. The $xy$ dimensions of the mesh are the bounding box of the deposited area, with an optional extension $\Delta x_s$ further into the substrate. The $z$ dimension of the mesh is 12.5 mm. The finest hex8 elements in the deposition region are 0.0368 mm × 0.0219 mm × 0.0224 mm respectively in the $x$, $y$, and $z$ dimensions. These dimensions are roughly 1/4 of the laser spot size, rounded such that a whole number of octree elements fill the domain. Elements coarsen away from the deposition region one octree generation at a time. Further details on the meshing are available in reference [43]. Because only one layer of build plate heating is studied, the mesh does not change in time.

Results on the sensitivity with respect to the substrate extension $\Delta x_s$ are shown in Fig. 7(a), which plots the predicted melt-pool volume with respect to the cumulative laser scan distance under different $\Delta x_s$. At the point of peak melt volume, the difference between cases H-a and H-b is about 2.4%. By further increasing $\Delta x_s$ from 1 mm to 5 mm, case H-b shows almost no change in melt pool volume either at the peak point or during the first bead (distance 0–5 mm) compared to H-c. Through the course of the second bead (distance 5–10 mm), case H-a diverges from the others, but H-b and H-c remain similar with no visual difference.

Next, we consider how the number of fine layers $n$ affects the model prediction. As shown in Fig. 7(b), doubling the number of fine layers to 8 for case H-d showed negligible difference compared to the default 4 layers for case H-a except for the peak melt volume. At the point of peak melt volume, the difference between cases H-a and H-d is only 3.6%. From the meshing study in cases H-a through H-d, it can be concluded that 4 fine layers is sufficient, but $\Delta x_s = 1$ mm substrate extension should be investigated further with other power control strategies (see cases 10-b and 10-c discussed in Sec. 4.1.5).

#### 4.1.3. Goldak parameter sensitivity

Next, heat source parameters such as Godak depth and efficiency are calibrated based on the melt-pool width and depth from the experiment measurements. The single track case D under a constant laser power of 250 W is chosen to be used for the calibration due to several reasons described as follows. First, overlapping melt pools in multi-track samples make it difficult to accurately determine the melt-pool boundary of an individual track. Further, the other single track experimental cases at 800 mm/s speed (standard laser scan speed of EOSINT), such as cases A and G, did not have any valid samples.

Goldak's ellipsoidal heat source $Q$ [38] is:

$$Q = \frac{6\sqrt{3}P\eta}{wdlr^3\pi\sqrt{\pi}} \exp\left( -\frac{3x^2}{w^2r^2} - \frac{3y^2}{d^2r^2} - \frac{3(z+vt)^2}{l^2r^2} \right) \tag{7}$$

where $\eta$ is the efficiency; $r$[m] is the radius; and $w$, $d$, and $l$ [dimensionless] are the width, depth, and length factors respectively of the ellipsoid. The local coordinate system $x$, $y$, $z$ is centered at each track.

Experimental samples D (D-1, D-2, D-3, and D-4) have a measured width of 151.4 ± 9 $\mu$m and measured depth of 95.6 ± 7.7 $\mu$m. Case D-a corresponds to using the nominal Goldak parameters of $d = 0.6$ and

**Table 4**
Description of the simulation cases studied for experimental validation.

| Case ID | Substrate extension $\Delta x_s$ (mm) | Number of fine layers $n$ | Goldak depth $d$ (dimensionless) | Goldak efficiency $\eta$ | Conductivity multiplication factor | Power profile | Number of tracks | Track length (mm) |
|---|---|---|---|---|---|---|---|---|
| D-a | 0 | 4 | 0.6 | 0.4 | 4 | Constant | 1 | 10 |
| D-b | 0 | 4 | 1.4 | 0.8 | 4 | Constant | 1 | 10 |
| D-c | 0 | 4 | 0.6 | 0.4 | 1 | Constant | 1 | 10 |
| D-d | 0 | 4 | 0.6 | 0.4 | 16 | Constant | 1 | 10 |
| H-a | 0 | 4 | 0.6 | 0.4 | 4 | Constant | 2 | 5 |
| H-b | 1 | 4 | 0.6 | 0.4 | 4 | Constant | 2 | 5 |
| H-c | 5 | 4 | 0.6 | 0.4 | 4 | Constant | 2 | 5 |
| H-d | 0 | 8 | 0.6 | 0.4 | 4 | Constant | 2 | 5 |
| 10-a | 0 | 4 | 0.6 | 0.4 | 4 | FEA | 5 | 5 |
| 10-b | 1 | 4 | 0.6 | 0.4 | 4 | FEA | 5 | 5 |
| 10-c | 1 | 4 | 1.4 | 0.8 | 4 | FEA | 5 | 5 |

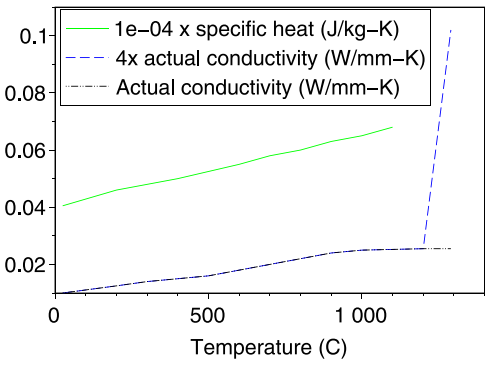


**Fig. 4.** Temperature-dependent thermal material properties for Inconel®625, including the actual conductivity (for case D-c only) and 4x actual conductivity for Marangoni modelling.

$\eta = 0.4$. Then a full-factorial study was conducted with 5 different heat source depths $d \in \{0.6, 0.8, 1.0, 1.2, 1.4\}$ and 6 different heat source absorption efficiencies $\eta \in \{0.4, 0.6, 0.7, 0.8, 0.9, 1.0\}$. To maintain the recommended four elements along each ellipse axis [39], the $z$ dimension of elements is increased proportionately with the heat source depth.

The results are shown in Fig. 8. Among all combinations of Goldak parameters, the case that has the closest match with the experimental measurements on the melt-pool width and depth corresponds to Goldak depth factor $d = 1.4$ and efficiency $\eta = 0.8$, which is named case D-b in Table 4. Simulation case D-b predicts the melt-pool to have a width of 148 $\mu$m and depth of 90.7 $\mu$m.

Fig. 9 shows the comparison of the experimental cross-section of sample D-1 (with a melt-pool width of 148 $\mu$m and depth of 90.7 $\mu$m) versus the simulations (inlaid) from cases D-a and D-b. With the nominal Goldak parameters, case D-a is similar in some ways to the Rosenthal solution, where the temperatures are too high at the center of the melt pool because the weld pool energy is concentrated at the weld center. Increasing the Goldak depth factor to 1.4 and efficiency $\eta = 0.8$ for case D-b reduces peak temperature and distributes energy away from the center. Nevertheless, case D-b has an unrealistically high efficiency. Simulating the true physics of melt-pool would require fluid dynamics. However, Sec. 4.1.5 will show that fluid dynamics are unnecessary for the FEA model-based control in this paper, as the tuned model produces a power profile that is nearly identical to the power profile generated from the nominal case D-a.

#### 4.1.4. *Marangoni effect*

In weld modelling, using artificially high thermal conductivity

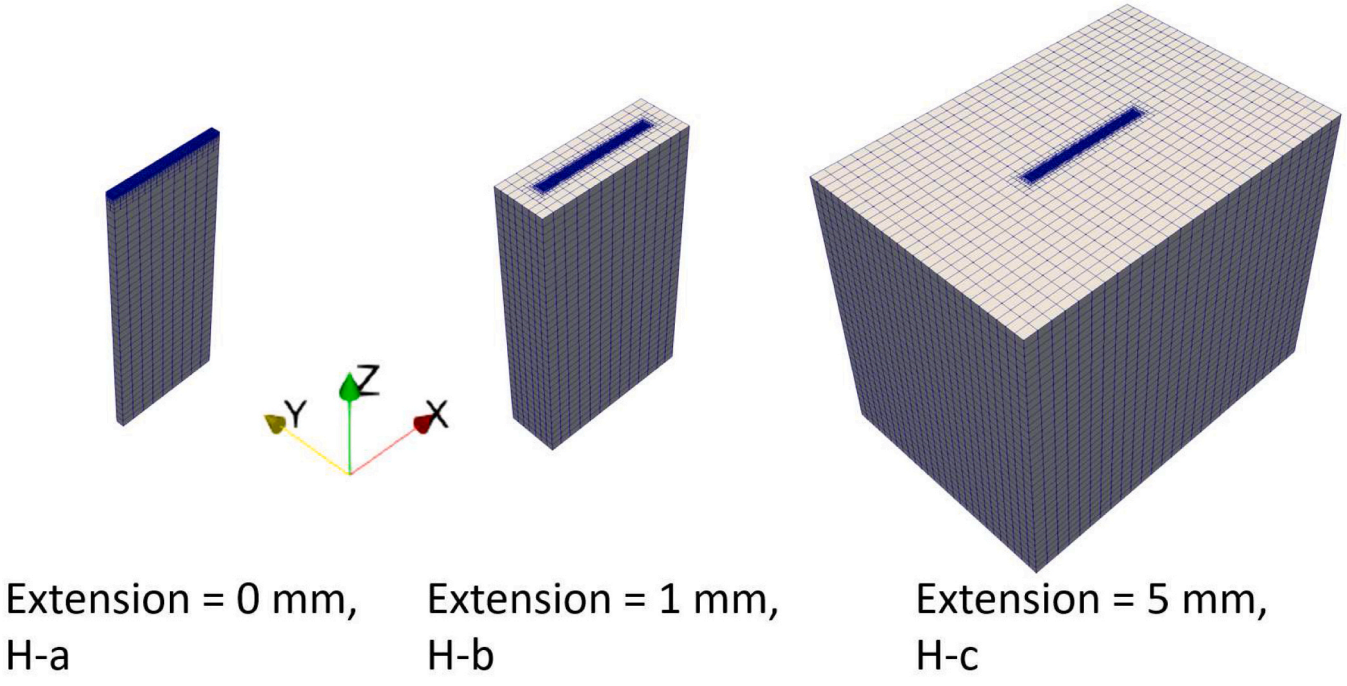


**Fig. 5.** Size of the simulation domain extending into the substrate for cases H-a, H-b, and H-c.

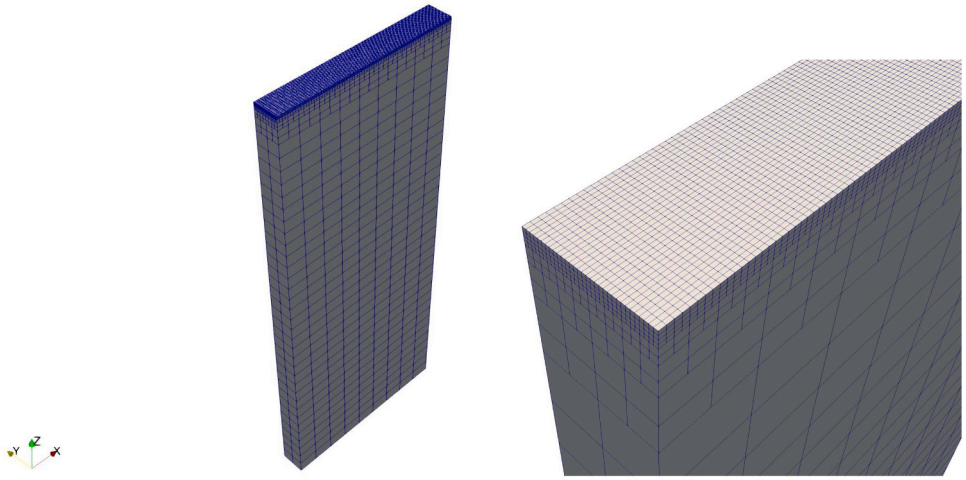

(a) Computational domain (b) Detailed view of 6(a)

**Fig. 6.** Hex8 mesh for 2 beads, each 5 mm long, case H-a, showing $n = 4$ fine layers.

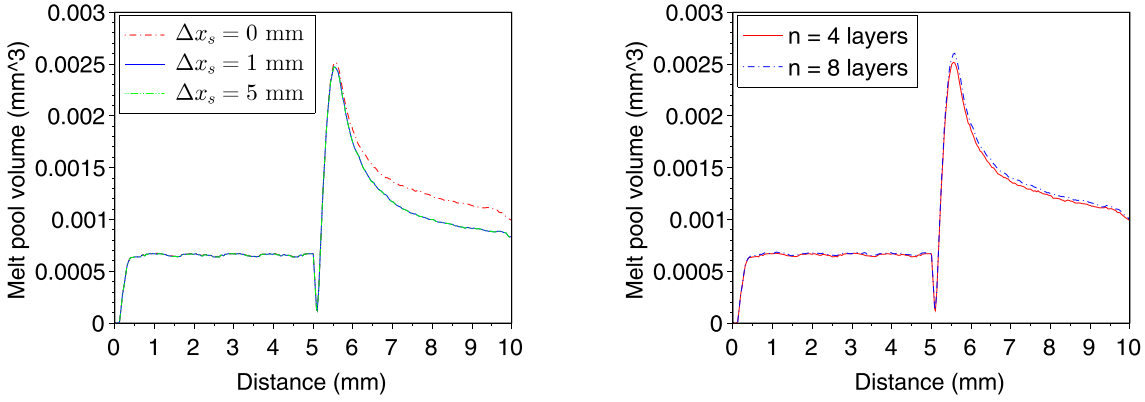


(a) Cases H-a ($\Delta x_s = 0$ mm), H-b ($\Delta x_s = 1$ mm), and H-c ($\Delta x_s = 5$ mm) (b) Cases H-a ($n = 4$) and H-d ($n = 8$)

**Fig. 7.** Sensitivity of simulated melt-pool volume with respect to substrate extension $\Delta x_s$ 7(a) and number of fine layers $n$ 7(b).

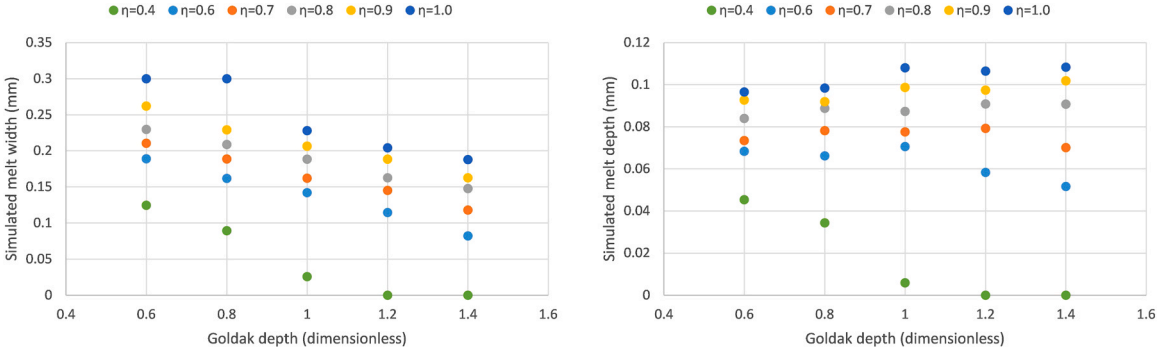


(a) Width (b) Depth

**Fig. 8.** Sensitivity of Goldak depth $d$ and efficiency $\eta$ on simulated melt pool width 8(a) and depth 8(b).

properties is a common practice to emulate the Marangoni effect [39,40]. For case D-a, conductivity above melting is left at the commonly used 4x nominal conductivity as shown in Fig. 4. Fig. 10 shows that using 1x conductivity for case D-c increased melt volume slightly, but mainly in the $x$ direction, with less than a 7% difference in the $y$ and $z$ directions. Increasing to 16x conductivity for case D-d makes the simulated melt pool even smaller.

#### 4.1.5. Sensitivity of FEA controlled power profile to simulation parameters

Till this end, the sensitivity study suggests that 4 fine layers and

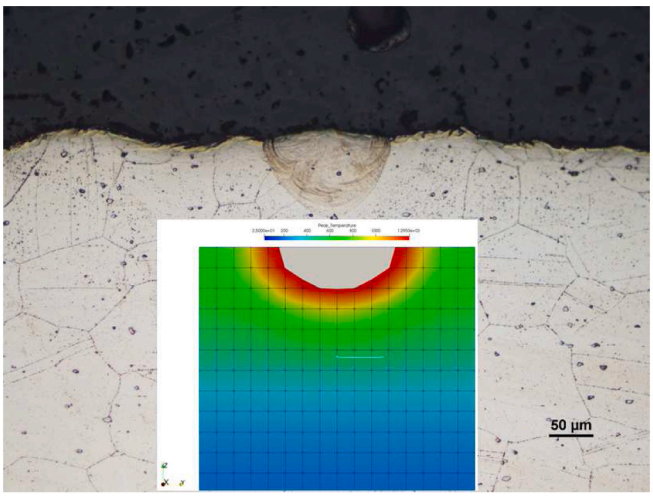


(a) Nominal case D-a, simulated width = 0.125 mm, depth = 0.0454 mm

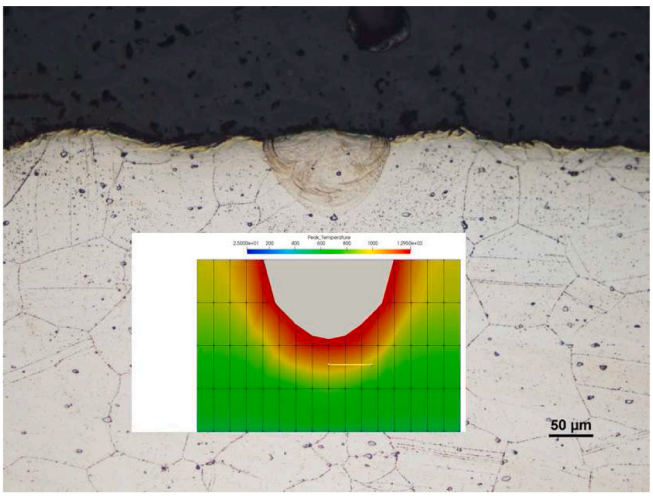


(b) Tuned case D-b, simulated width = 0.148 mm, depth = 0.0907 mm

**Fig. 9.** Experimental cross-section and simulations (inlaid) with nominal Goldak parameters 9(a) and Goldak depth factor $d = 1.4$ and efficiency $\eta = 0.8$ 9(b).

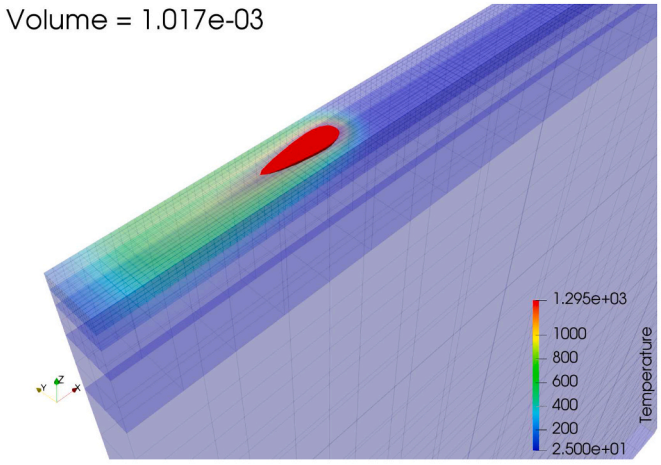


(a) Conductivity scaling 1x, case D-c

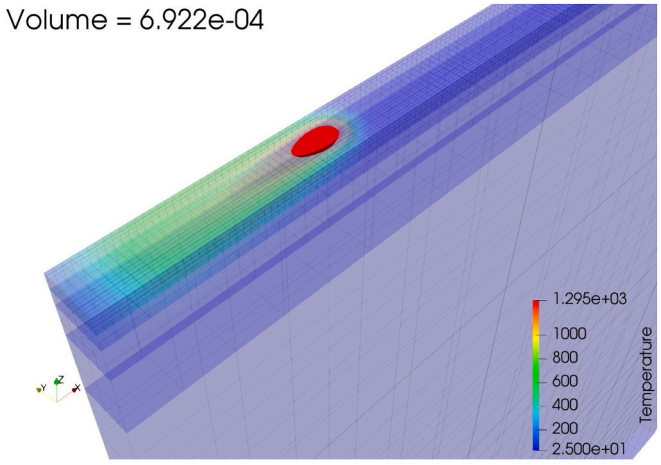


(b) Conductivity scaling 4x, case D-a

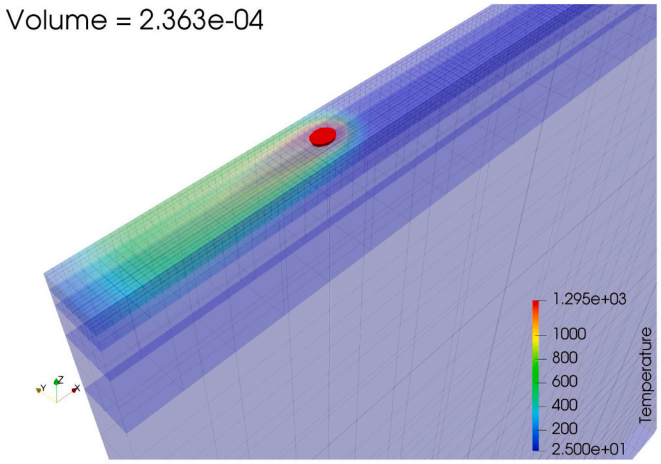


(c) Conductivity scaling 16x, case D-d

**Fig. 10.** Sensitivity of conductivity scaling factors on melt pool shapes (opaque), showing decreasing volumes with larger conductivities.

conductivity multiplication factor of 4 for Marangoni modeling are sufficient, but the substrate extension of $\Delta x_s = 1.0$ mm as well as the Goldak parameters of $d = 1.4$ and $\eta = 0.8$ need to be further investigated for a different laser power profile than constant. Hence, this subsection evaluates how the substrate extension and Goldak parameters would affect the resulting FEA controlled laser power profile for one of the most complicated sample configurations, 5-tracks with 5 mm track-length, as shorter track length can cause higher thermal buildup. Such evaluation corresponds to cases 10-a to 10-c in Table 4 and the corresponding simulated power profiles for the FEA controller are plotted in Fig. 11.

In Fig. 11(a), extending the simulated substrate by 1 mm (case 10-b) produces larger powers in the controlled power profile compared to the power profile using the nominal simulation parameters (case 10-a). The greatest difference in powers is in the 5th (final) track, which is on the edge and thus most affected by the boundary conditions. The difference in powers could also be due to errors which accumulate with time. Further increasing the substrate extension to $\Delta x_s = 5$ mm, similar to case H-c, increased computation times without significantly changing the results (not shown here due to the limited space). In Fig. 11(b), tuning the Goldak depth and efficiency cancels out the effects of substrate extension, bringing the power just below that of the nominal power profile (case 10-a).

In summary, both the nominal case 10-a and the tuned case 10-c produce the same qualitative trend in the controlled power profiles, while the Goldak parameters of the tuned model case 10-c are physically unrealistic. Therefore, the nominal simulation parameters defined in Sec. 4.1.1, consisting of $\Delta x_s = 0$, Goldak depth $d = 0.6$, efficiency $\eta = 0.4$, 4 fine layers, and conductivity multiplication factor of 4, were used to generate the FEA-controlled laser power profiles for experimental validation.

### 4.2. Numerical verification of power control

A representative case, 2-track with 10 mm track length under the standard scan speed of $v = 800$ mm/s, is selected here for a more in-depth numerical evaluation of the FEA power control. Figs. 12 and 13 show the comparison among three laser-power strategies: constant power profile (experimental case E), FEA controlled power profile (case 5), and analytic controlled power profile (case 7) from reference [31].

The increase in melt pool size for the 2nd bead under the constant laser power, illustrated in Fig. 12(a), indicates the need for controlling the laser power to attain a constant melt-pool size. The FEA control generates a constant melt-pool volume during the entire simulated build process of the two-track part. However, Fig. 12(b) shows that the melt-pool cross-sectional areas under the FEA controller are not exactly constant, especially there is a sudden increase in the melt-pool area at the beginning of the second bead. Fig. 13 plots the melt-pool cross-sections at 1 mm from the track end, corresponding to $x = 1$ mm and $x = 9$ mm.

Note that although the melt-pool volume under the FEA controller is maintained constant, the melt pool is changing shape during the simulated build process, as illustrated in Fig. 14. Fig. 14(a)-14(b) show the melt-pool shapes and volumes at the beginning of the second hatch with the laser at $x = 9.925$ mm. Then Fig. 14(c)-14(d) show the melt-pools at $x = 9.588$ mm when the melt-pool volume under the constant power reaches its maximum, which is about 2.5 times the volume at $x = 9.925$ mm. Between $x = 9.925$ and 9.588 mm, the melt-pool shape under each power profile shows an elongation along the scanning direction. Since the melt-pool volume under the FEA controlled power remains almost the same from $x = 9.925$–9.588 mm, the cross-sectional area in the $yz$ plane has increased. Fig. 14(e)-14(f) show the melt-pools around the midpoint of the second hatch ($x = 4.30$ mm), when the melt-pool under the constant power has nearly returned to its steady-state volume, which is still higher than its steady-state value at the end of the first hatch, about $0.7 \times 10^{-3} mm^3$ as indicated by Fig. 12(a).

Fig. 13(f) shows that the analytic controller from [31] has mitigated the increase of the melt-pool cross-sectional area at the laser returning point for scanning the second hatch ($x = 9$ mm), but it has over-compensated, leading to a reduced melt-pool cross-sectional area. By observing the melt-pool volume/area and the laser power profile shown in Fig. 12, it is noticed that the oscillation of the melt-pool volume/area at laser turnaround was partly due to that the analytic controller did not increase the laser power to compensate for the cooling during the skywriting time between the two hatches. In addition, the analytic controller was not able to regulate the melt-pool volume/area of the second hatch to the same steady-state value of the first hatch. However, since the analytic controller was designed based on a different model on melt-pool dynamics than FEA, it might not be fair to compare the performance of the analytic controller versus the FEA controller in terms of the FEA simulation.

In summary, the FEA controller of laser power based on the secant iterative method has achieved its goal of producing constant melt-pool volume. However, due to the change of melt-pool shape at the laser turnarounds, the melt-pool cross-sectional area varies at these local vicinities but otherwise rather flat. To the best knowledge of the authors, it is not clear so far to the AM research community which objective (either melt-pool volume or cross-sectional area) should be kept constant during the build process to lead to the best build quality, and additional investigation along this line is needed in the future.

### 4.3. Experimental validation of FEA power control

As described in Sec. 3, the laser power profiles generated by the FEA

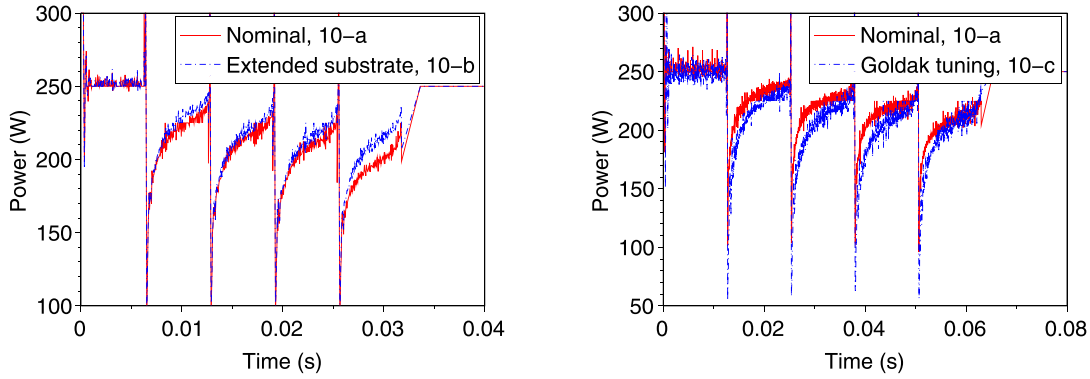


(a) Nominal (case 10-a) vs substrate extension only (case 10-b)

(b) Nominal (case 10-a) vs substrate extension and Goldak depth and efficiency tuning (case 10-c)

**Fig. 11.** Sensitivity of substrate extension and Goldak depth and efficiency on computed power profile to attain constant melt pool size.

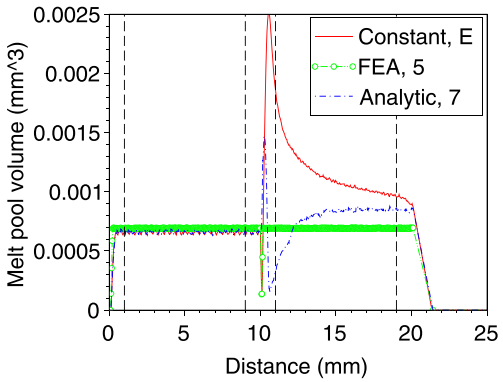


(a) Melt pool volume vs cumulative laser scan distance

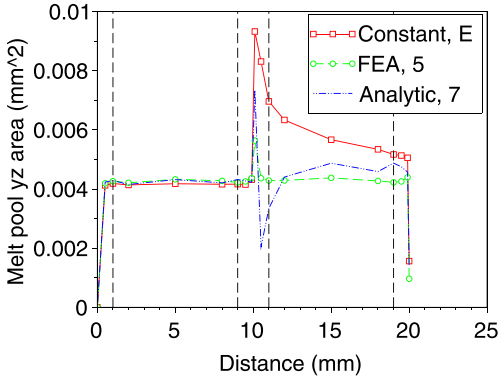


(b) Area vs distance

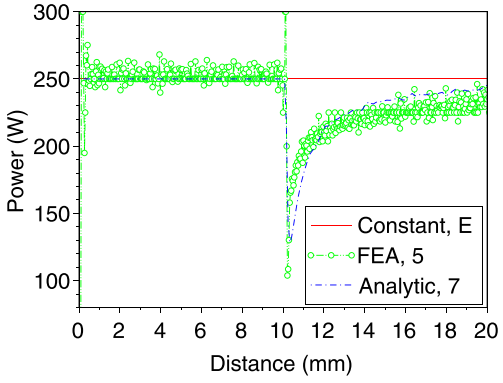


(c) Power vs distance. Markers on FEA data represent each time step mapped to laser scan distance.

**Fig. 12.** Simulated melt pool volumes, areas, and power profiles for each control strategy (cases E, 5, and 7) at 800 mm/s, 10 mm long, with 2 beads. Black dashed lines indicate the position of cross-sections 1 mm from track end.

with the secant iterative method were implemented on the EOSINT M280 to build samples. The experimental results of the FEA control are then quantified in Table 5, compared to the analytic controller [31] and the constant power cases. Several representative cross-sections and plots are shown in Figs. 15–16, and a significant outlier is shown in Fig. 17. In Figs. 15–16, the area measurements for the FEA controlled cases are offset horizontally such that the error bars are visible in the plots. In reality, the FEA measurements are taken at exactly the same location as the nominal measurements, 1 mm from the start and end of each track.

In Table 5, missing and obscured data are represented by "-". As shown in Table 3, there are no valid samples on the analytic controller for 2-bead parts with $L = 10$ mm and $v = 600$ mm/s. For 2-bead or 5-bead samples with 5 mm track length built under the constant laser power of 250 W and scan speed of 600 mm/s (samples Q's and R's), missing data are due to missing or obscured melt-pools whose boundaries cannot be identified. For example, as shown in Fig. 18, sample Q-2 bottom only has 1 visible melt pool, although there should be 2 tracks. Deep penetration, indicating an onset of keyhole, is observed for samples Q. In sample R-1 bottom as shown in Fig. 16, melt pools 2 and 6 are almost entirely obscured by neighboring melt pools due to severe overmelting.

The reference melt-pool cross-sectional area $A_{\text{ref}}$ for a particular scan speed $v$ and track length $L$ is defined as the average cross-sectional area of the single-bead constant-power builds for that speed and length. The error rate $e$ is defined as the average relative error compared to the reference melt-pool cross-sectional area $A_{\text{ref}}$:

$$e = \text{average}_i\left(\left|\frac{A_i - A_{\text{ref}}}{A_{\text{ref}}}\right|\right) \tag{8}$$

where $A_i$ are the measured melt-pool cross-sectional areas for all repetitions of an experiment. The amplification ratio $r_{\text{amp}}$ is defined as the maximum relative error compared to the reference melt-pool cross-sectional area, normalized such that 1 means no amplification:

$$r_{\text{amp}} = \max_i\left(\frac{A_i - A_{\text{ref}}}{A_{\text{ref}}}\right) + 1 \tag{9}$$

The attenuation ratio $r_{\text{att}}$ is defined as the minimum relative error compared to the reference melt-pool cross-sectional area:

$$r_{\text{att}} = \min_i\left(\frac{A_i - A_{\text{ref}}}{A_{\text{ref}}}\right) + 1 \tag{10}$$

The average, min, and max operations are performed over either 16 or 40 data points, depending on the case. Each experiment is repeated four times and each bead has two cross sections (1 mm from each track end). This gives 16 data points for the 2-bead experiments and 40 data points for the 5-bead experiments. For an ideal, perfectly controlled build with no variation in cross-sections, the optimal error rate would be 0, while the optimal amplification and attenuation ratios would be 1.

Two of the constant-power cases have attenuation ratios $r_{\text{att}}$ which are much less than 1. There is no clear reason why a constant-power multi-bead case would be attenuated compared to a single-bead. For case O (600 mm/s, 5 tracks, 10 mm), the attenuation ratio $r_{\text{att}} = 0.6424$ is attributed to sample O-4 bottom, melt pool #3, as shown in Fig. 17. All of the case O samples have some degree of attenuation, but sample O-4 bottom has the most extreme outlier. This extremity dominates the minimum ratio $r_{\text{att}}$ in Table 5. Some cases, like O-1 top in Fig. 16(b), have relatively consistent melt pool cross-sectional areas. The drastic variation in melt pool cross-sectional areas between identical samples could be due to stochastic factors in the process, such as melt pool turbulence, inconsistent surface finish, or material non-homogeneity. Although these factors are difficult to control, they could be addressed to some extent by process monitoring and stochastic control [45]. Another factor which cannot be easily controlled is the effect of optics on the melt pool shape. Minor beam distortions will occur at the periphery of the processing area. The utilized EOSINT M280 system is equipped with an f-theta lens with a focal length > 400 mm. At the build plate, the measured, resulting laser beam (second moment) diameter is 74.5 $\mu$m, with a Rayleigh range extending several millimeters. Given this focusing geometry, it is estimated that any distortions of the beam will be less than 5% and are negligible.

Both the FEA and analytic controllers successfully decrease the error rate $e$ compared to applying the constant power for all cases. In addition, both controllers decrease the amplification ratio $r_{\text{amp}}$ compared to using the constant power for all cases. Nevertheless, both controllers decrease the attenuation ratio $r_{\text{att}}$ compared to applying the constant power for all cases, indicating that they have overcompensated at some of the measurement points. For the case of $v = 800$ mm/s, $L = 10$ mm, and 2-track, the FEA controller has a lower error rate than the analytic controller, but

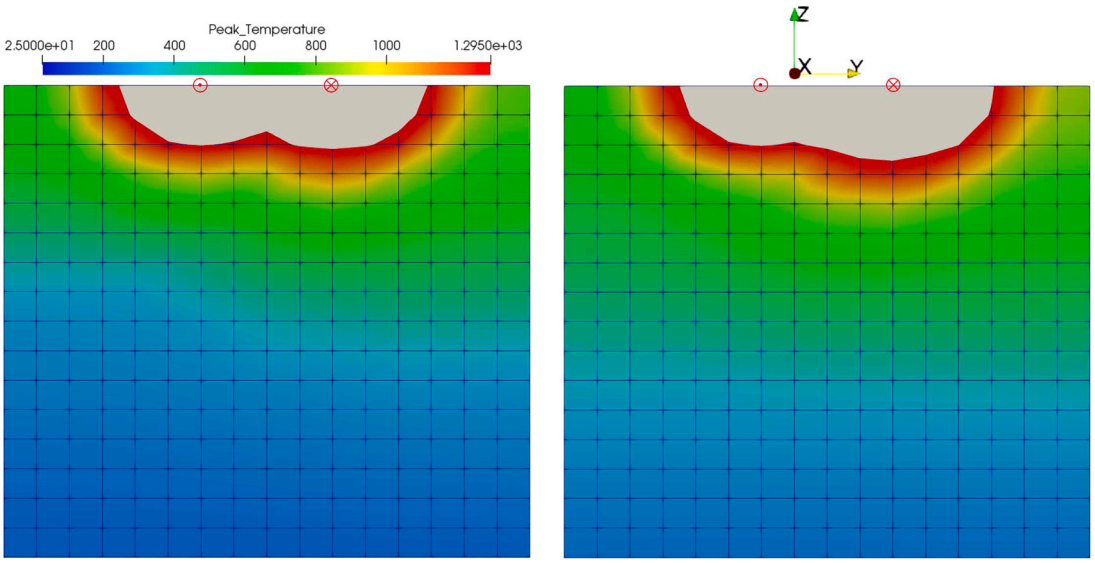


(a) $x = 1$ mm, constant case E (b) $x = 9$ mm, constant case E

(c) $x = 1$ mm, FEA case 5 (d) $x = 9$ mm, FEA case 5

(e) $x = 1$ mm, analytic case 7 (f) $x = 9$ mm, analytic case 7

**Fig. 13.** Simulated melt pool cross sections at 800 mm/s, 10 mm long, with 2 beads, and no substrate extension. Asymmetry of cross-section is most pronounced in 13(a), while 13(b) shows improvement. There appears to be overcompensation in 13(c), but this may be due to different model assumptions.

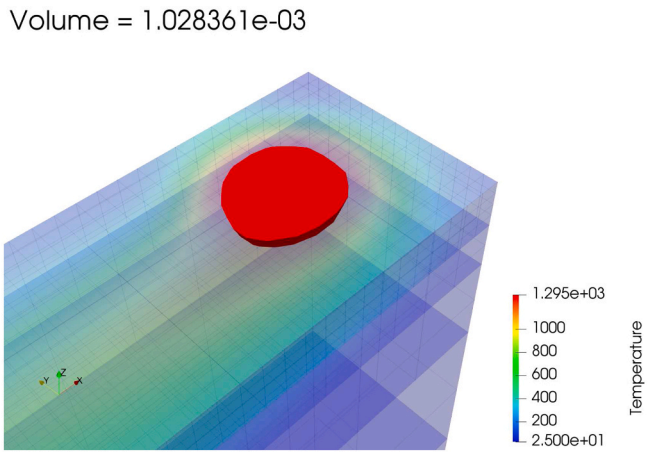


(a) Constant, case E, laser position $x = 9.925$ mm in the second hatch, width = 0.184 mm, depth = 0.0514 mm, length = 0.201 mm

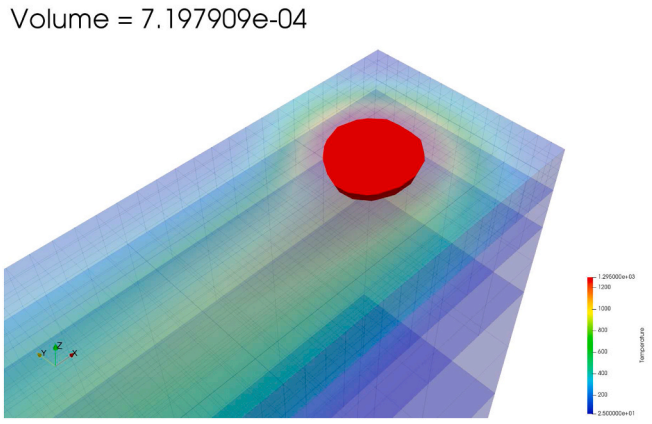


(b) FEA, case 5, $x = 9.925$ mm in the second hatch, width = 0.168 mm, depth = 0.0469 mm, length = 0.178 mm

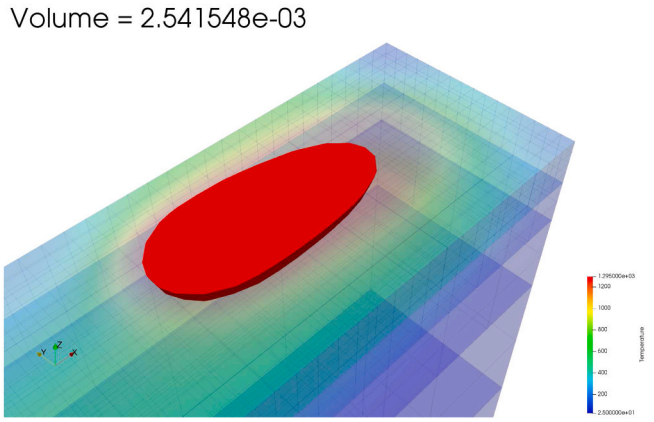


(c) Constant, case E, $x = 9.588$ mm in the second hatch, width = 0.184 mm, depth = 0.0666 mm, length = 0.399 mm

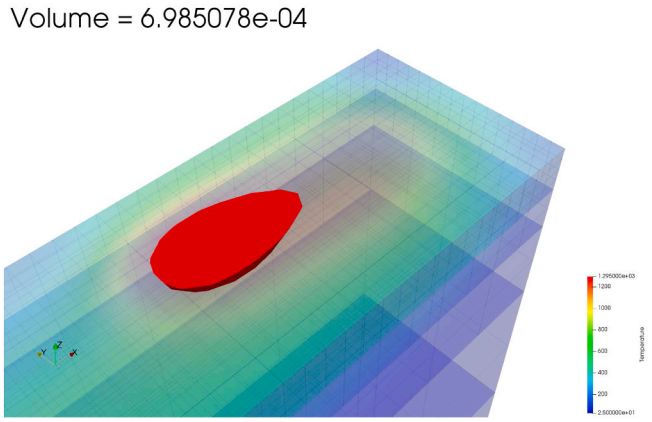


(d) FEA, case 5, $x = 9.588$ mm in the second hatch, width = 0.132 mm, depth = 0.0449 mm, length = 0.246 mm

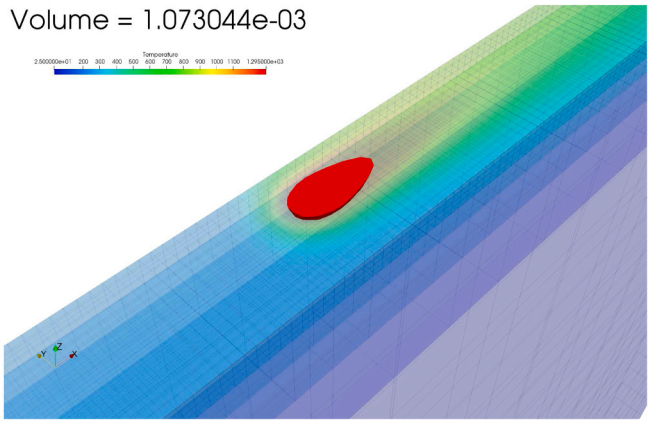


(e) Constant, case E, $x = 4.30$ mm in the second hatch, width = 0.148 mm, depth = 0.0490 mm, length = 0.304 mm

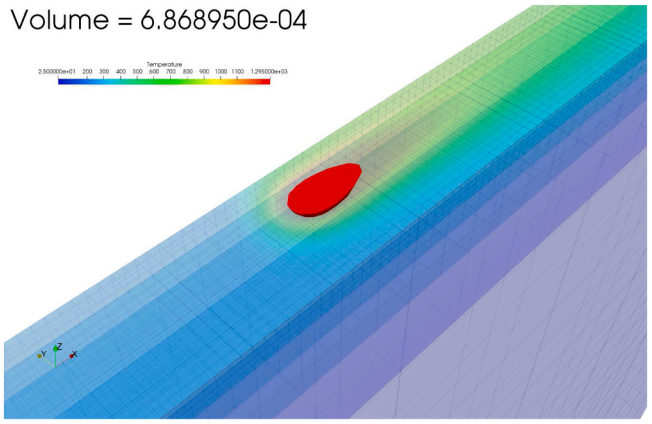


(f) FEA, case 5, $x = 4.30$ mm in the second hatch, width = 0.125 mm, depth = 0.0454 mm, length = 0.256 mm

**Fig. 14.** Simulated melt pool volumes (opaque, red) with temperature results (semi-transparent) at 800 mm/s, 10 mm long, with 2 beads, at several critical locations under the constant power (left, case E) and FEA controlled power (right, case 5). Laser position $x = 9.925$ mm is at the beginning of the second hatch, $x = 9.588$ mm is when the constant power case reaches maximum volume, and $x = 4.30$ mm is roughly the middle of the second hatch when both cases are nearly back to steady-state. (For interpretation of the references to colour in this figure legend, the reader is referred to the web version of this article.)

**Table 5**
Average error rate, peak amplification ratio, and peak attenuation ratio of the FEA control compared to the analytic control [31] and the constant power cases.

| Configuration | $A_{ref}$ (um$^2$) | Tracks | $e$ | | | $r_{amp}$ | | | $r_{att}$ | | |
|---|---|---|---|---|---|---|---|---|---|---|---|
| | | | Constant | Analytic | FEA | Constant | Analytic | FEA | Constant | Analytic | FEA |
| v = 800 mm/s | 10267.55 | 2 | 0.2588 | 0.1481 | 0.1325 | 1.6437 | 1.0103 | 1.3753 | 1.0021 | 0.6789 | 0.7827 |
| L = 10 mm | | 5 | 0.2590 | 0.1984 | 0.2242 | 1.6513 | 1.0498 | 1.0114 | 0.6387 | 0.4825 | 0.5590 |
| v = 600 mm/s | 16013.59 | 2 | 0.1935 | – | 0.1533 | 1.4041 | – | 1.0622 | 0.5604 | – | 0.6555 |
| L = 10 mm | | 5 | 0.2519 | 0.1476 | 0.2098 | 1.8258 | 1.2212 | 1.3612 | 0.6424 | 0.5110 | 0.5579 |
| v = 600 mm/s | 16844.66 | 2 | – | 0.2126 | 0.2385 | – | 0.9079 | 0.8594 | – | 0.6960 | 0.6387 |
| L = 5 mm | | 5 | – | 0.2815 | 0.3255 | – | 0.9814 | 0.8585 | – | 0.4846 | 0.4579 |

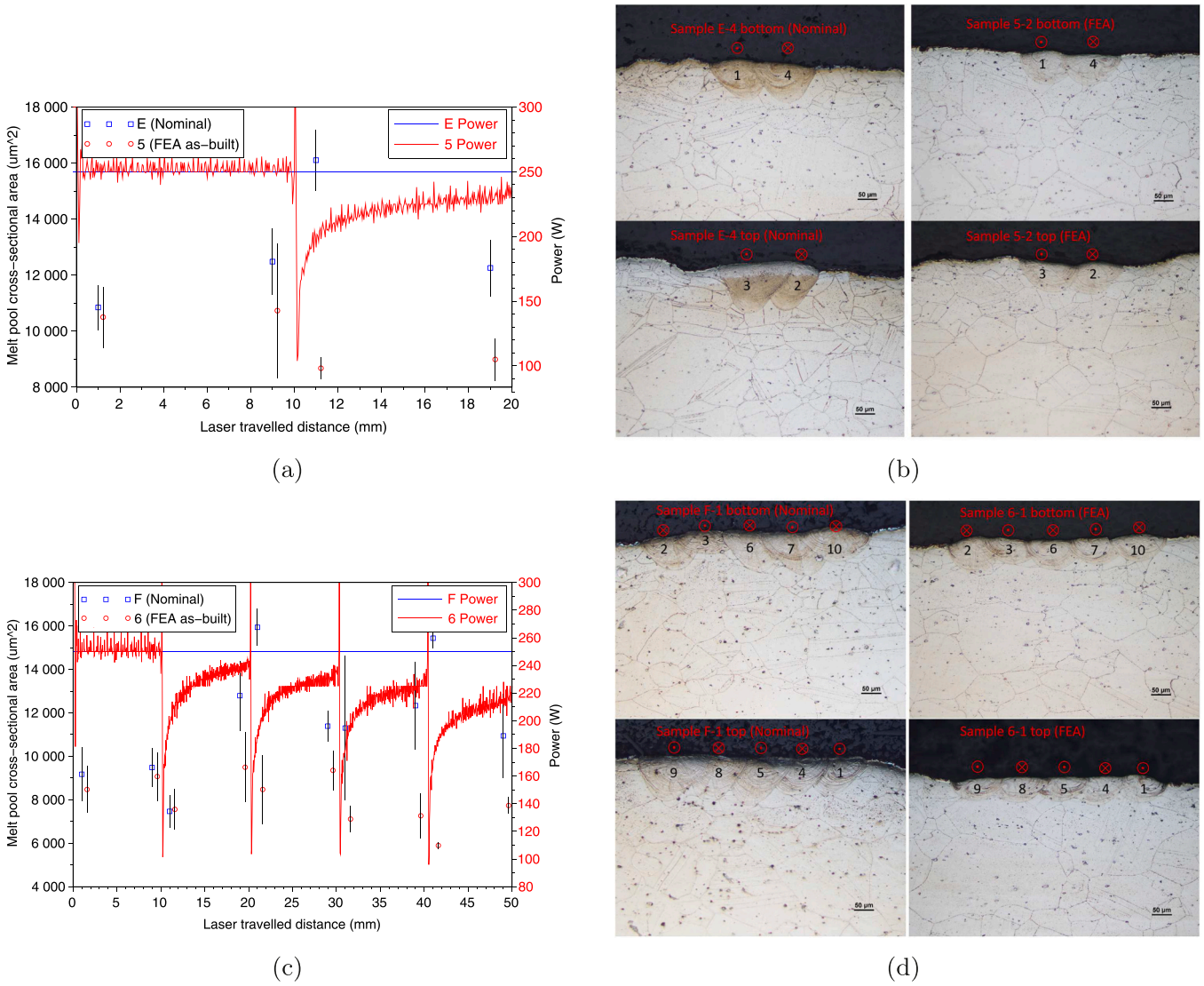


**Fig. 15.** Average melt pool cross-sectional area with error bars indicating standard deviation across repeated samples under the nominal constant-power and FEA-controlled-power with $L = 10$ mm, $v = 800$ mm/s, 2 tracks 15(a) and 5 tracks 15(b). Power inputs to the machine are shown on the right axis. The numerical sequence labeled on the melt-pool image represents the sequence of laser scanning, and the top and bottom cross-sections of each sample represent the two cross-section cuts at 1 mm from each track end. ⊗ or ⊙ denotes the laser has traversed into or out of the page, respectively.

has a higher error rate in some other cases. The analytic controller has a lower $r_{att}$ than the FEA controller in more cases, indicating a more frequently over-compensation in laser power.

It is worth pointing out that the analytic controller was designed to directly control the melt-pool cross-sectional area [31] whereas the FEA controller is designed to regulate the melt-pool volume, which attributes to the performance degradation, to a certain extent, when the validation is performed with respect to the cross-sectional area. Again, as acknowledged earlier in the paper, it is not clear whether maintaining a constant melt-pool volume would lead to a better build quality compared to maintaining a constant melt-pool cross-sectional area. This paper adopted melt-pool volume as a representative metric, but the same methodology can be equally applied to another geometric variable such as cross-sectional area or depth if later research proves it is needed. Existing studies often correlate the conduction mode or keyhole mode with the melt-pool width-to-depth ratio [46], where the ideal conduction mode is defined for the width-to-depth equal to 2, and the melt-pool is considered under keyholing if the width-to-depth ratio is significantly

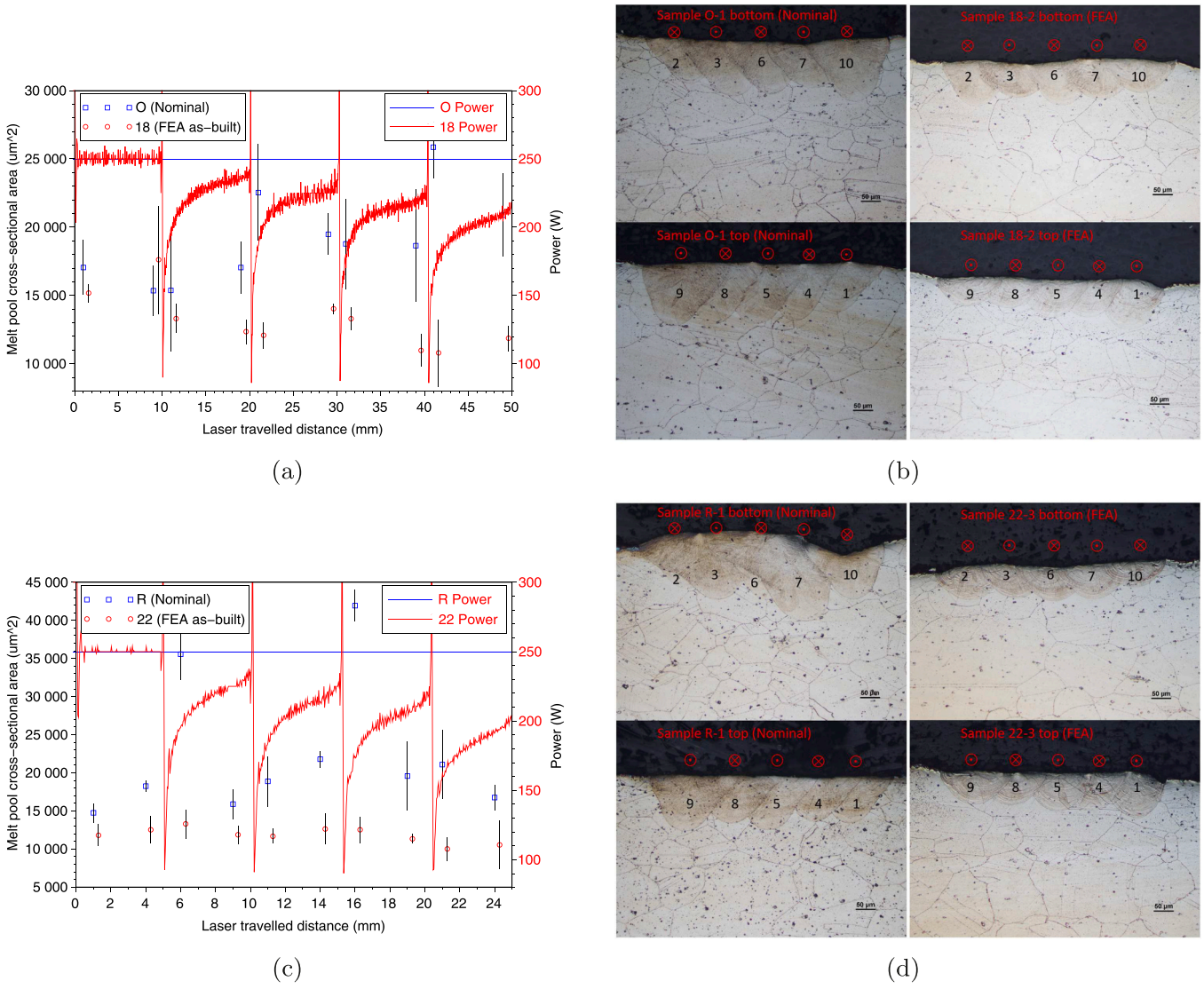


**Fig. 16.** Average melt pool cross-sectional area and standard deviation for samples under the nominal constant-power and FEA-controlled-power with $v = 600$ mm/s, 5 tracks, $L = 10$ mm 16(a) and $L = 5$ mm 16(c). Power inputs to the machine are shown on the right axis. The numerical sequence labeled on the melt-pool images represents the sequence of laser scanning, and the top and bottom cross-sections of each sample represent the two cross-section cuts at 1 mm from each track end. ⊗ or ⊙ on each melt-pool image denotes that the melt-pool has traversed into or out of the page, respectively.

smaller than 2 (or depth-to-width ratio significantly larger than 2). Table 6 summarizes the average (and standard deviation) of melt-pool width-to-depth ratio under all controllers. For all except the case (800 mm/s, 10 mm, 2-tracks), the melt-pool width-to-depth ratio under the FEA controller is closer to the ideal conduction-mode ratio of 2 than the analytic controller. For all cases, the FEA and analytic controllers have improved the melt-pool width-to-depth ratio, making it closer to 2 compared to applying the constant power.

Overall, the FEA controller and the analytic controller demonstrate similar control performance for the simple multi-hatch builds in this study. However, the analytic controller developed in [31] is only applicable to simple builds with straight hatches. The FEA controller is more easily extended to large toolpaths for real parts. Future work will include demonstrations with more realistic, complex parts.

### 4.4. Computation cost

The FEA simulation for the case of 2-tracks, 5 mm track length, with constant power (case H-a) takes 5 min 56 s wall time on a 28 core system operating at 2.60 GHz. With iterative simulation (case 9), it takes 13 min 40 s. Larger simulations take longer, as both the number of elements and the number of time steps increase. For the case of 5-tracks and 20 mm track length (case 2), iterative simulation takes 16 hr 26 min and a maximum of 915 MB RAM usage.

## 5. Conclusions

This paper developed a secant-based iterative method for controlling the simulated laser power and implemented it with the FEA model to maintain a constant melt pool volume during the simulated build process. A set of experiments was designed and built to evaluate the effectiveness of the FEA controller, by implementing the laser-power profiles generated from the FEA controller on an EOSINT M280 LPBF system.

The experiments showed that the FEA controller was effective at producing more consistent melt pool cross-sections compared to applying a constant power (default value of 250 W was used by the EOSINT M280 system), especially for reducing the melt-pool volume at laser turnarounds during the scanning of multi-track samples caused by repeatedly heating the same track end. Nevertheless, overcompensation

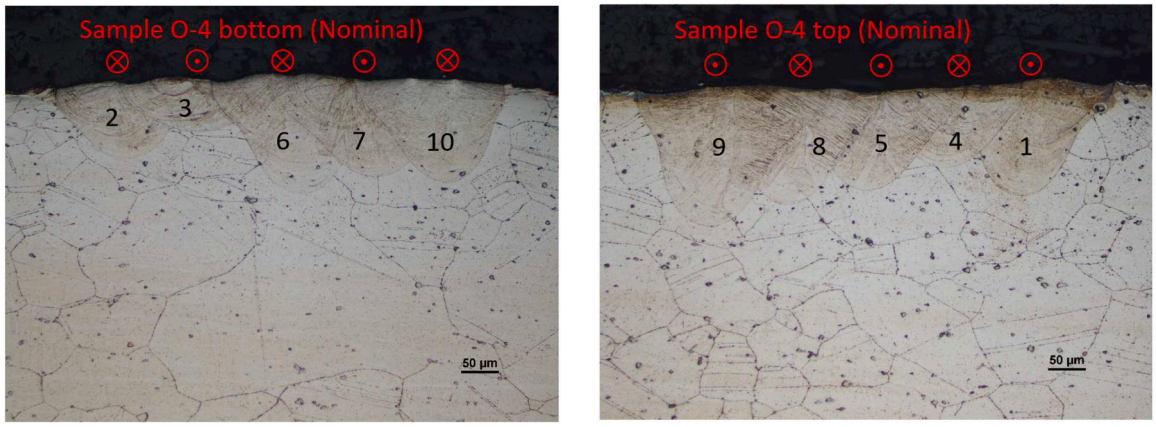


**Fig. 17.** Melt pool #3 has the smallest cross-sectional area out of all the samples for case O; the numerical sequence labeled on the melt-pool image represents the sequence of laser scanning, and the top and bottom cross-sections of each sample represent the two cross-section cuts at 1 mm from each track end. ⊗ or ⊙ on each melt-pool image denotes that the melt-pool has traversed into or out of the page, respectively.

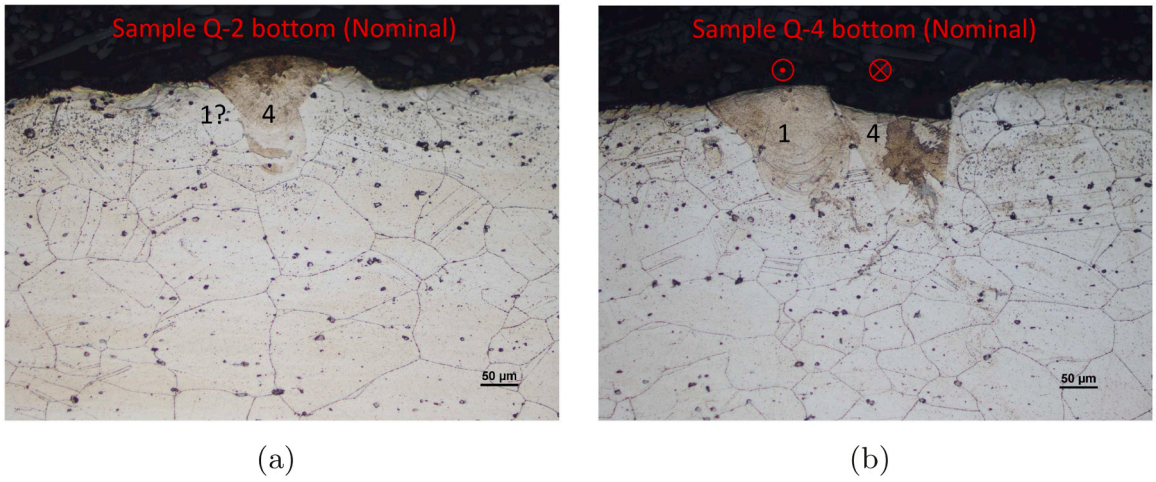


**Fig. 18.** Deep penetration observed in sample Q-2 18(a) (only 1 melt pool is visible) and sample Q-4 18(b).

**Table 6**
Melt-pool width-to-depth of the FEA control compared to the analytic control [31].

| Configuration | Tracks | Constant | Analytic | FEA |
|---|---|---|---|---|
| v = 800 mm/s, | 2 | 1.47 ± 0.17 | 1.84 ± 0.17 | 1.70 ± 0.20 |
| L = 10 mm | 5 | 1.83 ± 0.55 | 2.04 ± 0.43 | 2.05 ± 0.29 |
| v = 600 mm/s, | 5 | 1.51 ± 0.30 | 1.65 ± 0.27 | 1.72 ± 0.26 |
| L = 10 mm | | | | |
| v = 600 mm/s, L = 5 mm | 2 | – | 1.69 ± 0.15 | 1.75 ± 0.26 |
| | 5 | - | 1.88 ± 0.25 | 1.94 ± 0.21 |

was sometimes observed that rendered the melt-pool cross-sections at laser turnarounds smaller than its reference value. Part of the control errors were due to that the FEA controller was designed to attain a constant melt-pool volume, rather than a constant melt-pool cross-sectional area, which was used for experimental validation. Simulations showed that although the melt-pool size was maintained constant, due to the melt-pool shape change at the beginning and end of each hatch, the melt-pool cross-sectional area varied at these locations.

Future work could include controlling other objectives, such as melt cross-sectional area or depth instead of melt volume. Other process variables could be designed, such as scan speed or hatch ordering instead of just power. The same control strategies could be applied to larger parts instead of small 5-hatch bead-on-plate melting. Sensitivity analysis or a better volume quadrature could be used to produce a smoother FEA power profile with faster computational times.

Finally, although this work focuses on turnarounds in small toolpaths, it could also be applied to reducing defects at overhangs as in references [22,23]. In reference [47], a 6.3 mm by 6.3 mm by 38 layer part is simulated with a moving source model. This size is roughly the limit of toolpaths that could be optimized with full geometric fidelity. For larger parts, this controller could be coupled with lookup tables based on average temperature of the previous layer, scan length, and other variables for feature-based transfer of control strategies, similar to the work by Druzgalski et al. [22].

## CRediT authorship contribution statement

**Jeff E. Irwin**: Methodology, Software, Writing - original draft, Visualization. **Qian Wang:** Conceptualization, Writing - review & editing. **Panagiotis (Pan) Michaleris:** Conceptualization, Software, Writing - review & editing. **Abdalla R. Nassar:** Methodology, Investigation, Validation, Writing - review & editing. **Yong Ren:** Formal analysis, Data curation. **Christopher B. Stutzman:** Investigation.

## Declaration of Competing Interest

The authors declare that they have no known competing financial interests or personal relationships that could have appeared to influence the work reported in this paper.

## Acknowledgments

This work was supported in part by the U.S. National Science Foundation under Grant 2015930.

## References

[1] A. Cutolo, B. Neirinck, K. Lietaert, C. de Formanoir, B. Van Hooreweder, Influence of layer thickness and post-process treatments on the fatigue properties of cocr scaffolds produced by laser powder bed fusion, Addit. Manuf. 23 (2018) 498–504.
[2] C. Tan, S. Li, K. Essa, P. Jamshidi, K. Zhou, W. Ma, M.M. Attallah, Laser powder bed fusion of ti-rich tini lattice structures: process optimisation, geometrical integrity, and phase transformations, Int. J. Mach. Tools Manuf. 141 (2019) 19–29.
[3] Z. Snow, A. Nassar, E.W. Reutzel, Review of the formation and impact of flaws in powder bed fusion additive manufacturing, Addit. Manuf. (2020), 101457.
[4] N. Levkulich, S. Semiatin, J. Gockel, J. Middendorf, A. DeWald, N. Klingbeil, The effect of process parameters on residual stress evolution and distortion in the laser powder bed fusion of ti-6al-4v, Addit. Manuf. 28 (2019) 475–484.
[5] W.E. King, H.D. Barth, V.M. Castillo, G.F. Gallegos, J.W. Gibbs, D.E. Hahn, C. Kamath, A.M. Rubenchik, Observation of keyhole-mode laser melting in laser powder-bed fusion additive manufacturing, J. Mater. Process. Technol. 214 (2014) 2915–2925.
[6] M. Tang, P.C. Pistorius, J. Beuth, Prediction of lack-of-fusion porosity for powder bed fusion, Addit. Manuf. 14 (2017) 39–48.
[7] H. Gong, K. Rafi, H. Gu, T. Starr, B. Stucker, Analysis of defect generation in ti–6al–4v parts made using powder bed fusion additive manufacturing processes, Addit. Manuf. 1 (2014) 87–98.
[8] G. Kasperovich, J. Haubrich, J. Gussone, G. Requena, Correlation between porosity and processing parameters in tial6v4 produced by selective laser melting, Mater. Des. 105 (2016) 160–170.
[9] L. Zhou, H. Hyer, S. Park, H. Pan, Y. Bai, K.P. Rice, Y. Sohn, Microstructure and mechanical properties of zr-modified aluminum alloy 5083 manufactured by laser powder bed fusion, Addit. Manuf. 28 (2019) 485–496.
[10] Y. Tian, J. Muñiz-Lerma, M. Brochu, Nickel-based superalloy microstructure obtained by pulsed laser powder bed fusion, Mater. Charact. 131 (2017) 306–315.
[11] A., Vasinonta, J., Beuth, M., Griffith, Process maps for controlling residual stress and melt pool size in laser-based sff processes 200, in: 2000 International Solid Freeform Fabrication Symposium, (2000).
[12] F. Imani, A. Gaikwad, M. Montazeri, P. Rao, H. Yang, E. Reutzel, Process mapping and in-process monitoring of porosity in laser powder bed fusion using layerwise optical imaging, J. Manuf. Sci. Eng. 140 (2018).
[13] J.V. Gordon, S.P. Narra, R.W. Cunningham, H. Liu, H. Chen, R.M. Suter, J.L. Beuth, A.D. Rollett, Defect structure process maps for laser powder bed fusion additive manufacturing, Addit. Manuf. (2020), 101552.
[14] J., Beuth, J., Fox, J., Gockel, C., Montgomery, R., Yang, H., Qiao, E., Soylemez, P., Reeseewatt, A., Anvari, S., Narra, et al., Process mapping for qualification across multiple direct metal additive manufacturing processes, in: Solid freeform fabrication proceedings, Univ. Tex. Austin, (2013) pp. 655–665.
[15] T.G. Gallmeyer, S. Moorthy, B.B. Kappes, M.J. Mills, B. Amin-Ahmadi, A. P. Stebner, Knowledge of process-structure-property relationships to engineer better heat treatments for laser powder bed fusion additive manufactured inconel 718, Addit. Manuf. 31 (2020), 100977.
[16] A.J., Dunbar, A.R., Nassar, E.W., Reutzel, J.J., Blecher, A real-time communication architecture for metal powder bed fusion additive manufacturing, in: Solid Freeform Fabrication Symposium (SFF), Austin, TX, (2016) pp. 67–80.
[17] T. Craeghs, F. Bechmann, S. Berumen, J.-P. Kruth, Feedback control of layerwise laser melting using optical sensors, Phys. Procedia 5 (2010) 505–514.
[18] E. Toyserkani, A. Khajepour, A mechatronics approach to laser powder deposition process, Mechatronics 16 (2006) 631–641.
[19] L. Song, V. Bagavath-Singh, B. Dutta, J. Mazumder, Control of melt pool temperature and deposition height during direct metal deposition process, Int. J. Adv. Manuf. Technol. 58 (2012) 247–256.
[20] L. Tang, R.G. Landers, Melt pool temperature control for laser metal deposition processes – part i: online temperature control, J. Manuf. Sci. Eng. 132 (2010).
[21] J. Lee, V. Prabhu, Simulation modeling for optimal control of additive manufacturing processes, Addit. Manuf. 12 (2016) 197–203.
[22] C. Druzgalski, A. Ashby, G. Guss, W. King, T. Roehling, M. Matthews, Process optimization of complex geometries using feed forward control for laser powder bed fusion additive manufacturing, Addit. Manuf. (2020), 101169.
[23] H. Yeung, B. Lane, J. Fox, Part geometry and conduction-based laser power control for powder bed fusion additive manufacturing, Addit. Manuf. 30 (2019), 100844.
[24] X., Cao, B., Ayalew, Control-oriented mimo modeling of laser-aided powder deposition processes, in: 2015 American Control Conference (ACC), IEEE, (2015) pp. 3637–3642.
[25] X., Cao, B., Ayalew, Multivariable predictive control of laser-aided powder deposition processes, in: 2015 American Control Conference (ACC), IEEE, (2015) pp. 3625–3630.
[26] Q. Wang, J. Li, M. Gouge, A.R. Nassar, P.P. Michaleris, E.W. Reutzel, Physics-based multivariable modeling and feedback linearization control of melt-pool geometry and temperature in directed energy deposition, J. Manuf. Sci. Eng. 139 (2017), 021013.
[27] Q. Wang, J. Li, A.R. Nassar, E.W. Reutzel, W.F. Mitchell, Model-based feedforward control of part height in directed energy deposition, Materials 14 (2021) 337.
[28] A. Papacharalampopoulos, P. Stavropoulos, J. Stavridis, Adaptive control of thermal processes: laser welding and additive manufacturing paradigms, Procedia CIRP 67 (2018) 233–237.
[29] S.A. Khairallah, A.A. Martin, J.R. Lee, G. Guss, N.P. Calta, J.A. Hammons, M. H. Nielsen, K. Chaput, E. Schwalbach, M.N. Shah, Controlling interdependent meso-nanosecond dynamics and defect generation in metal 3d printing, Science 368 (2020) 660–665.
[30] D. Rosenthal, Mathematical theory of heat distribution during welding and cutting, Weld. J. 20 (1941) 220–234.
[31] Q. Wang, P.P. Michaleris, A.R. Nassar, J.E. Irwin, Y. Ren, C.B. Stutzman, Model-based feedforward control of laser powder bed fusion additive manufacturing, Addit. Manuf. 31 (2020), 100985.
[32] H. Sieurin, R. Sandström, Austenite reformation in the heat-affected zone of duplex stainless steel 2205, Mater. Sci. Eng. A 418 (2006) 250–256.
[33] J. Li, Q. Wang, P.P. Michaleris, E.W. Reutzel, A.R. Nassar, An extended lumped-parameter model of melt–pool geometry to predict part height for directed energy deposition, J. Manuf. Sci. Eng. 139 (2017).
[34] A.S. Azar, S.K. Ås, O.M. Akselsen, Determination of welding heat source parameters from actual bead shape, Comput. Mater. Sci. 54 (2012) 176–182.
[35] J. Li, Q. Wang, An analytical computation of temperature field evolved in directed energy deposition, J. Manuf. Sci. Eng. 140 (2018).
[36] P. Michaleris, Modeling metal deposition in heat transfer analyses of additive manufacturing processes, Finite Elem. Anal. Des. 86 (2014) 51–60.
[37] J. Song, J. Shanghvi, P. Michaleris, Sensitivity analysis and optimization of thermo-elasto-plastic processes with applications to welding side heater design, Comput. Methods Appl. Mech. Eng. 193 (2004) 4541–4566.
[38] J. Goldak, A. Chakravarti, M. Bibby, A new finite element model for welding heat sources, Metall. Trans. B 15 (1984) 299–305.
[39] J. Goldak, M. Bibby, J. Moore, R. House, B. Patel, Computer modeling of heat flow in welds, Metall. Trans. B 17 (1986) 587–600.
[40] M. Gouge, P. Michaleris. Thermo-Mechanical Modeling of Additive Manufacturing, Butterworth-Heinemann, 2017.
[41] N. Contuzzi, S. Campanelli, A. Ludovico, 3d finite element analysis in the selective laser melting process, Int. J. Simul. Model. (IJSIMM) 10 (2011).
[42] W. Goodell, J. Coulter, P. Johnson, Optical constants of inconel alloy films, JOSA 63 (1973) 185–188.
[43] C. Li, E.R. Denlinger, M.F. Gouge, J.E. Irwin, P. Michaleris, Numerical verification of an octree mesh coarsening strategy for simulating additive manufacturing processes, Addit. Manuf. 30 (2019), 100903.
[44] J. Ning, D.E. Sievers, H. Garmestani, S.Y. Liang, Analytical modeling of in-situ deformation of part and substrate in laser cladding additive manufacturing of inconel 625, J. Manuf. Process. 49 (2020) 135–140.
[45] B. Yao, F. Imani, H. Yang, Markov decision process for image-guided additive manufacturing, IEEE Robot. Autom. Lett. 3 (2018) 2792–2798.
[46] J. Elmer, W. Giedt, T. Eagar, The transition from shallow to deep penetration during electron beam welding, Weld. J. 69 (1990) 167s–175s.
[47] E.R. Denlinger, M. Gouge, J. Irwin, P. Michaleris, Thermomechanical model development and in situ experimental validation of the laser powder-bed fusion process, Addit. Manuf. 16 (2017) 73–80.